Local and global magnetization on the Sierpiński carpet

Jozef Genzor,[1,2,3] Andrej Gendiar [iD],[4] and Tomotoshi Nishino[1]

[1]*Department of Physics, Graduate School of Science, Kobe University, Kobe 657-8501, Japan*
[2]*Physics Division, National Center for Theoretical Sciences, Taipei 10617, Taiwan*
[3]*Physics Division, National Center for Theoretical Sciences, National Taiwan University, Taipei 10617, Taiwan*
[4]*Institute of Physics, Slovak Academy of Sciences, Dúbravská Cesta 9, SK-845 11 Bratislava, Slovakia*

The phase transition of the classical Ising model on the Sierpiński carpet, which has the fractal dimension $\log_3 8 \approx 1.8927$, is studied by an adapted variant of the higher-order tensor renormalization group method. The second-order phase transition is observed at the critical temperature $T_c \approx 1.478$. Position dependence of local functions is studied through impurity tensors inserted at different locations on the fractal lattice. The critical exponent β associated with the local magnetization varies by two orders of magnitude, depending on lattice locations, whereas T_c is not affected. Furthermore, we employ automatic differentiation to accurately and efficiently compute the average spontaneous magnetization per site as a first derivative of free energy with respect to the external field, yielding the global critical exponent of $\beta \approx 0.135$.

I. INTRODUCTION

The understanding of phase transitions and critical phenomena plays an important role in condensed matter physics [1]. Systems on regular lattices are the major target of such studies, where elementary models exhibit translationally invariant states, which are scale invariant at criticality. It has been known that critical behavior is controlled by global properties, such as dimensionality and symmetries. This is the concept of *universality*.

If we focus our attention on inhomogeneous lattices, there is a group of fractal lattices which are self-similar and exhibit noninteger Hausdorff dimensions. Geometrical details, such as lacunarity and connectivity, could thus modify the properties of their critical phenomena. An important aspect of the fractal lattices is the ramification, which is the smallest number of bonds that have to be cut to isolate an arbitrarily large bounded subset surrounding a point. In early studies by Gefen *et al.* [2–5], it was shown that the short-range classical spin models on finitely ramified lattices exhibit no phase transition at nonzero temperature.

The ferromagnetic Ising model on the fractal lattice that corresponds to the Sierpiński carpet is one of the most extensively studied models with fractal lattice geometry. Monte Carlo studies combined with the finite-size scaling method have been performed [6–11], including the Monte Carlo renormalization group (RG) method [12]. The critical temperature T_c is relatively well estimated within the narrow range $1.47 \lesssim T_c \lesssim 1.50$, where one of the most recent estimates is $T_c = 1.495(5)$ by Bab *et al.* [11]. On the other hand, estimates of critical exponents are still fluctuating, since it is rather hard to collect sufficient numerical data for a precise finite-size scaling analysis [13]. This is partially so because an elementary lattice unit can contain too many sites, and there are a variety of choices with respect to boundary conditions. This situation persists even in a recent study by means of a path-counting approach [14]. Yet, a number of issues remain unresolved concerning uniformity of fractal systems in the thermodynamic limit [10].

Recently, we showed that the higher-order tensor renormalization group (HOTRG) method [15] can be used as an appropriate numerical tool for studies of certain types of fractal systems [16–19]. The method is based on the real-space RG and, therefore, the self-similar property of fractal lattices can be treated in a natural manner. In this paper, we apply the HOTRG method to the Ising model on the fractal lattice that corresponds to the Sierpiński carpet. The method enables us to estimate T_c from the temperature dependence of the entanglement entropy $s(T)$. To check the uniformity in the thermodynamic functions, we choose three distinct locations on the lattice and calculate the local magnetization $m(T)$ and the bond energy $u(T)$. As trivially expected, these local functions, $m(T)$ and $u(T)$, yield the identical T_c. Contrary to the naive intuition, the critical exponent β, which is associated with the local magnetization $m(T) \propto (T_c - T)^\beta$, strongly depends on the location of measurement, and the estimated exponent β can vary within two orders of magnitude with respect to the three different locations on the fractal lattice, where the local functions are calculated.

Recent research has demonstrated the effectiveness of automatic differentiation, a technique derived from deep learning, for accurately and efficiently computing higher-order derivatives in tensor network algorithms [20,21]. Automatic differentiation is based on a computation graph representing the sequence of elementary computation steps in a directed acyclic graph. This technology can propagate gradients with machine precision throughout the computation process. In tensor network algorithms, the implementation of numerically stable differentiation through linear algebra operations, such as singular value decomposition (SVD), is crucial. By applying automatic differentiation to our tensor network fractal, we can accurately calculate the average spontaneous
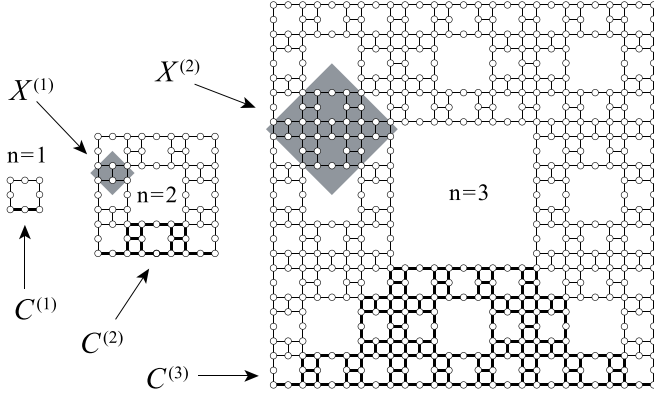
044108-1

FIG. 1. Buildup process of a discrete analog of the Sierpiński carpet. The circles represent the lattice points where the Ising spins are located. The vertical and horizontal links denote the interacting pairs. The first three units $n = 1, 2,$ and 3 are shown. For each unit n, we draw the corners $C^{(n)}$ by thick lines. We label the shaded regions $X^{(1)}$ and $X^{(2)}$.

magnetization as the first derivative of the free energy with respect to the external field. Unlike numerical derivatives, this approach avoids introducing numerical errors due to finite step sizes. Once the magnetization is computed, we can extract the global critical exponent β.

The structure of this paper is as follows. In the next section, we explain the recursive construction of the fractal lattice and express the partition function of the system in terms of contractions among tensors. In Sec. III, we introduce the HOTRG method for the purpose of keeping the numerical cost realistic. The way of measuring the local functions $m(T)$ and $u(T)$ is explained. Numerical results are shown in Sec. IV. Position dependence of the local functions is observed. In the last section, we summarize the obtained results and discuss the reason for the pathological behavior of the fractal system.

II. MODEL REPRESENTATION

There are several different types of discrete lattices that can be identified as the Sierpiński carpet. Among them, we choose the one constructed by the extension process shown in Fig. 1. In the first step ($n = 1$), there are eight spins in the unit, as shown on the left. The Ising spins $\sigma = \pm 1$ are represented by the circles and the ferromagnetic nearest-neighbor interactions are denoted by the horizontal and vertical lines. In the second step ($n = 2$), the eight units are grouped to form a new extended unit, as shown in the middle. Now, there are 64 spins on the 9×9 square lattice grid. On the right side, we show the third step ($n = 3$). Generally, in the nth step, an extended unit contains 8^n spins on the $3^n \times 3^n$ lattice. The Hausdorff dimension of this lattice is $d_{\mathrm{H}} = \log_3 8 \approx 1.8927$ in the thermodynamic limit $n \to \infty$.

In the series of the extended units we have thus constructed, there is another type of recursive structure. In Fig. 1 at the bottom of each unit, we have drawn a pyramidlike area by the thick lines. One can identify four such pyramidlike areas within each unit (enumerated by n), and each area can be called the *corner* $C^{(n)}$. The corners are labeled $C^{(1)}$, $C^{(2)}$, and $C^{(3)}$ from left to right therein. It should be noted that there are
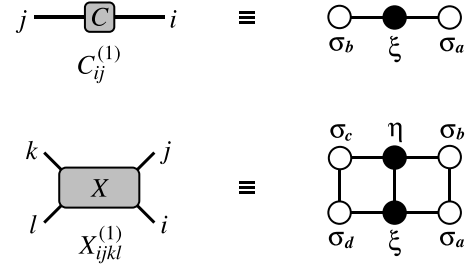

FIG. 2. Structure of the initial corner matrix $C_{ij}^{(1)}$ in Eq. (3) and the four-leg tensor $X_{ijkl}^{(1)}$ in Eq. (6).

only 2^{n-1} spin sites in common, where two adjacent corners meet.

In the case $n = 2$ drawn in the middle, we shaded a region on the left, which contains six sites, and label the region $X^{(1)}$. Having observed the corner $C^{(2)}$ at the bottom, we found that the corner consists of two rotated pieces of $X^{(1)}$ and four pieces of $C^{(1)}$. In $n = 3$, we shaded a larger region $X^{(2)}$ (in the similar manner as $X^{(1)}$), which now contains 36 sites. We can recognize that $X^{(2)}$ consists of seven pieces of $X^{(1)}$ and the two pieces of $C^{(1)}$. We have thus identified the following recursive relations, which build up the fractal:

(1) Each nth unit contains four pieces of $C^{(n)}$,

(2) $C^{(n+1)}$ contains two pieces of $X^{(n)}$ and four pieces of $C^{(n)}$,

(3) $X^{(n+1)}$ contains seven pieces of $X^{(n)}$ and two pieces of $C^{(n)}$.

The Hamiltonian of the Ising model, which is constructed on the series of finite-size systems $n = 1, 2, 3, \ldots$, has the form

$$H^{(n)} = -J \sum_{\langle ab \rangle} \sigma_a \sigma_b. \tag{1}$$

The summation runs over all pairs of the nearest-neighbor Ising spins, as shown by the circles in Fig. 1. The spin positions are labeled by the lattice indices a and b. They are connected by the lines, which correspond to the ferromagnetic interaction $J > 0$, and no external magnetic field is imposed. First, we calculate the partition function (expressed in arbitrary step n)

$$Z^{(n)} = \sum \exp\left[-\frac{H^{(n)}}{k_{\mathrm{B}} T}\right] \tag{2}$$

as a function of temperature T, where the summation is taken over all spin configurations and where k_{B} denotes the Boltzmann constant. At initial step $n = 1$, we define the *corner matrix*

$$C_{ij}^{(1)} = \sum_{\xi = \pm 1} \exp[K \xi (\sigma_a + \sigma_b)], \tag{3}$$

where $K = J/k_{\mathrm{B}} T$, and the matrix indices $i = (\sigma_a + 1)/2$ and $j = (\sigma_b + 1)/2$ take the value either 0 or 1. The structure on the right-hand side is graphically shown in Fig. 2 (top), and the summation taken over the spin ξ is denoted by the filled circle. We have chosen the ordering of the indices i and j, which is opposite if comparing $C_{ij}^{(1)}$ with the corresponding graph. The partition function of the smallest unit ($n = 1$), which contains
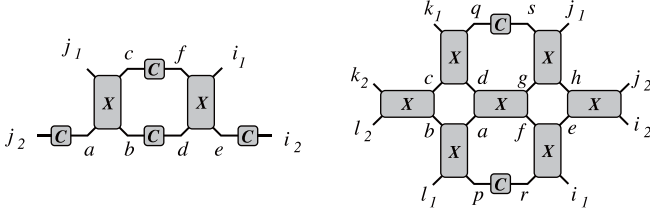
FIG. 3. Extension of the local matrix $C^{(n)}$ in Eq. (7) (on the left) and the tensor $X^{(n)}$ in Eq. (8) (on the right).

eight spins, is then expressed as

$$Z^{(1)} = \sum_{ijkl} C_{ij}^{(1)} C_{jk}^{(1)} C_{kl}^{(1)} C_{li}^{(1)}, \tag{4}$$

and can be abbreviated to $\text{Tr}\,[C^{(1)}]^4$. We will express $Z^{(n)}$ for arbitrary $n > 1$ in the same trace form

$$Z^{(n)} = \text{Tr}\,[C^{(n)}]^4 \tag{5}$$

by means of the corner matrix $C_{ij}^{(n)}$, where each one undergoes *extensions*, as we define in the following.

Let us notice that the region $X^{(1)}$ appears from the step $n = 2$. The Boltzmann weight corresponding to this region $X^{(1)}$ can be expressed by the four-leg (fourth-order) tensor

$$X_{ijkl}^{(1)} = \sum_{\xi\eta} \exp[K(\sigma_a\sigma_b + \sigma_c\sigma_d + \xi\eta)]$$

$$\times \exp[K\xi(\sigma_a + \sigma_d) + K\eta(\sigma_b + \sigma_c)], \tag{6}$$

where the spin locations are depicted in Fig. 2 (bottom). We have additionally introduced new indices $k = (\sigma_c + 1)/2$ and $l = (\sigma_d + 1)/2$. Now we can mathematically represent the recursive relations in terms of contractions among the matrices $C^{(n)}$ and tensors $X^{(n)}$. Figure 3 shows the graphical representation of the extension processes. Taking the contraction among the two tensors $X^{(n)}$ and the four matrices $C^{(n)}$, as shown in Fig. 3 (left), we obtain the *extended* corner matrix $C^{(n+1)}$ through the corresponding formula

$$C_{ij}^{(n+1)} = C_{(i_1 i_2)(j_1 j_2)}^{(n+1)}$$

$$= \sum_{abcdef} C_{aj_2}^{(n)} X_{abcj_1}^{(n)} C_{fc}^{(n)} C_{db}^{(n)} X_{dei_1 f}^{(n)} C_{i_2 e}^{(n)}, \tag{7}$$

where the new indices i and j, respectively, represent the grouped indices $(i_1 i_2)$ and $(j_1 j_2)$. Apparently, the diagram in Fig. 3 (left) is more convenient than Eq. (7) for the better understanding of the contraction geometry. This relation can be easily checked for the case $n = 1$ after comparing Figs. 1–3.

Similarly, the extension process from $X^{(n)}$ to $X^{(n+1)}$ shown in Fig. 3 (right) can be expressed by the formula

$$X_{ijkl}^{(n+1)} = X_{(i_1 i_2)(j_1 j_2)(k_1 k_2)(l_1 l_2)}^{(n+1)}$$

$$= \sum_{\substack{abcdef \\ ghprqs}} X_{abl_1 p}^{(n)} X_{bck_2 l_2}^{(n)} X_{cdqk_1}^{(n)} X_{fgda}^{(n)}$$

$$\times X_{efri_1}^{(n)} X_{ghj_1 s}^{(n)} X_{i_2 j_2 he}^{(n)} C_{rp}^{(n)} C_{sq}^{(n)}, \tag{8}$$

where we have again abbreviated the grouped indices to $i = (i_1 i_2)$, $j = (j_1 j_2)$, $k = (k_1 k_2)$, and $l = (l_1 l_2)$. This relation can be checked for the case $n = 1$ by comparing the area $X^{(1)}$ and $X^{(2)}$ in Fig. 1.

Through the iterative extension of the tensors, we can *formally* obtain the corner matrix $C_{ij}^{(n)}$ for arbitrary n, and express $Z^{(n)}$ by Eq. (5). The free energy per spin is then

$$f^{(n)} = -\frac{1}{8^n} k_B T \ln Z^{(n)} \tag{9}$$

since the nth unit contains 8^n spins. This function converges to a value $f^{(\infty)}$ in the thermodynamic limit $n \to \infty$, where convergence with respect to n is rapid, and $n = 35$ is sufficient in the numerical analyses. The specific heat per site can be evaluated by taking the second derivative of the free energy $c_f(T) = -T\frac{\partial^2}{\partial T^2}f^{(\infty)}$. Furthermore, the global spontaneous magnetization m_f can be evaluated as the first derivative of the free energy $f^{(\infty)}$ with respect to the external field h:

$$m_f(T) = -\frac{\partial f^{(\infty)}}{\partial h}\bigg|_{h\to 0}. \tag{10}$$

To avoid numerical errors due to the finite step as in the case of the numerical derivative, we calculate the global magnetization m_f according to the Eq. (10) accurately and efficiently using automatic differentiation applied to the tensor network program for the partition function of the fractal lattice in our study.

III. RENORMALIZATION GROUP TRANSFORMATION

The matrix dimension of $C^{(n)}$ is 2^{n-1} by definition. Therefore, it is impossible to keep all the matrix elements faithfully in numerical analysis, when n is large. The situation is more severe for $X^{(n)}$, which has four indices. By means of the HOTRG method [15], it is possible to reduce the tensor-leg dimension, the degree of freedom, down to a realistic number. The reduction process is performed by the RG transformation U, which is created from the higher-order SVD [22] applied to the extended tensor $X_{ijkl}^{(n+1)}$.

Suppose that the tensor-leg dimension in $X_{ijkl}^{(n)}$ is D for each index, i.e., $i, j, k, l = 0, 1, \ldots, D - 1$. As we have shown in Eq. (8), the dimension of the grouped index $i = (i_1 i_2)$ in $X_{(i_1 i_2)(j_1 j_2)(k_1 k_2)(l_1 l_2)}^{(n+1)}$ is equal to D^2. We reshape the four tensor indices to form a rectangular matrix with the grouped index $(i_1 i_2)$ and the remaining grouped index $(j_1 j_2 k_1 k_2 l_1 l_2)$ with the dimension D^6. Applying the SVD to the reshaped tensor, we obtain

$$X_{(i_1 i_2)(j_1 j_2 k_1 k_2 l_1 l_2)}^{(n+1)} = \sum_{\xi} U_{(i_1 i_2)\xi}\, \omega_\xi\, V_{(j_1 j_2 k_1 k_2 l_1 l_2)\xi}, \tag{11}$$

where U and V are generalized unitary, i.e., orthonormal, matrices $U^T U = V^T V = \mathbb{1}$. We assume the decreasing order for the singular values ω_ξ by convention. Keeping D dominant degrees of freedom for the index ξ at most, we regard the matrix $U_{(i_1 i_2)\xi}$ as the RG transformation from $(i_1 i_2)$ to the renormalized index ξ. For the purpose of clarifying the relation between the original pair of indices $(i_1 i_2)$ and the renormalized index ξ, we *rename* ξ to i and write the
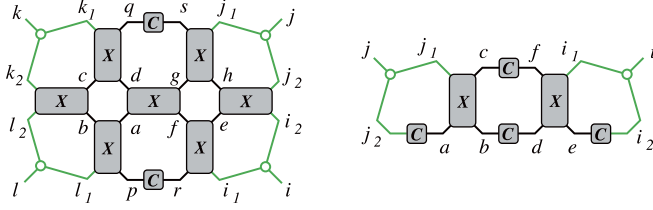
FIG. 4. The renormalization group transformations in Eq. (12) (on the left) and Eq. (13) (on the right) applied, respectively, to Eqs. (8) and (7) (cf. Fig. 3).

RG transformation as $U_{(i_1 i_2) i}$. In the same manner, we obtain $U_{(j_1 j_2) j}$, $U_{(k_1 k_2) k}$, and $U_{(l_1 l_2) l}$, where we have distinguished the transformation matrices by their indices.

The RG transformation is then performed as

$$X_{ijkl}^{(n+1)} \leftarrow \sum_{\substack{i_1 i_2 j_1 j_2 \\ k_1 k_2 l_1 l_2}} U_{(i_1 i_2) i} U_{(j_1 j_2) j} U_{(k_1 k_2) k} U_{(l_1 l_2) l}$$
$$\times X_{(i_1 i_2)(j_1 j_2)(k_1 k_2)(l_1 l_2)}^{(n+1)}, \tag{12}$$

where the sum is taken over the indices on the connected lines in Fig. 4 (left). The left arrow used in Eq. (12) represents the replacement of the expanded tensor $X_{(i_1 i_2)(j_1 j_2)(k_1 k_2)(l_1 l_2)}^{(n+1)}$ for the renormalized one $X_{ijkl}^{(n+1)}$. Since the RG transformation matrices U are obtained from SVD applied to $X_{(i_1 i_2)(j_1 j_2)(k_1 k_2)(l_1 l_2)}^{(n+1)}$, there is no guarantee that the RG transformation can be straightforwardly applied to $C_{(i_1 i_2)(j_1 j_2)}^{(n+1)}$, as we have defined in Eq. (7). It has been confirmed that the transformation

$$C_{ij}^{(n+1)} \leftarrow \sum_{\substack{i_1 i_2 \\ j_1 j_2}} U_{(i_1 i_2) i} U_{(j_1 j_2) j} C_{(i_1 i_2)(j_1 j_2)}^{(n+1)} \tag{13}$$

is of use in the actual numerical calculation. The corresponding diagram is shown in Fig. 4 (right).

We add a remark on the choice of the transformation matrix U. In a trial calculation, once we tried to create U from the corner matrix $C_{ij}^{(n+1)}$ by both SVD and diagonalization. However, we encountered numerical instabilities, in which the singular values (or eigenvalues) decayed to zero too rapidly, especially, when n was large. Thus, we always create U from SVD that is applied to $X_{ijkl}^{(n+1)}$ only.

With the use of these RG transformations, it is possible to repeat the extension processes in Eqs. (7) and (8), and to obtain a good numerical estimate for $Z^{(n)}$ and $f^{(n)}$ in Eq. (9). The actual numerical calculations in this paper were performed by a slightly modified procedure, which we describe in detail in the Appendix. We split $X_{ijkl}^{(n)}$ into two halves and represent each part by a three-leg tensor. This computational trick allowed us to increase the leg dimension up to $D = 30$ or even larger.

A. Impurity tensors

In the framework of the HOTRG method, thermodynamic functions, such as the magnetization per site $m(T)$ and the internal energy per bond $u(T)$, can be calculated from the free energy per site $f^{(\infty)}$. Alternatively, these functions are
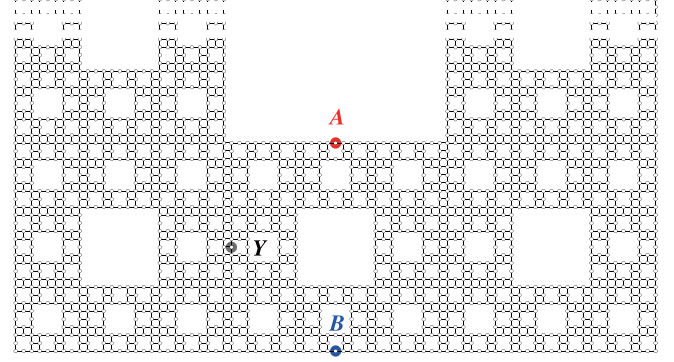

FIG. 5. Three positions A (on inner boundary), B (on outer boundary), and Y (in innermost position) chosen for the observation of local functions. The lower half of the unit $n = 4$ is drawn only.

obtained by inserting impurity tensors (separately derived from $C^{(n)}$ and $X^{(n)}$) into the tensor network of the entire system. Since the fractal lattice under consideration is inhomogeneous, these thermodynamic functions can depend on the position they are placed. To check the dependence, we choose three typical locations A, B, and Y, as shown in Fig. 5 on the fractal lattice.

As an example of such a single site function, let us consider a tensor representation of the local magnetization. Looking at the position of site A in Fig. 5, one finds that it is located on the corner matrix $C^{(1)}$. Thus, the initial impurity tensor on that location is expressed as

$$A_{ij}^{(1)} = \sum_{\xi = \pm 1} \xi \, \exp[K \xi (\sigma_i + \sigma_j)], \tag{14}$$

similar to Eq. (3). It is also easy to check that the initial impurity tensor $B^{(1)}$, which is placed on a position different from A, is expressed by the identical equation, so we have $A_{ij}^{(1)} = B_{ij}^{(1)}$. Site Y lies inside the area $X^{(1)}$ and we define the corresponding initial tensor for local magnetization as

$$Y_{ijkl}^{(1)} = \sum_{\xi \eta} \frac{\xi + \eta}{2} \exp[K (\sigma_i \sigma_j + \sigma_k \sigma_l + \xi \eta)]$$
$$\times \exp[K \xi (\sigma_j + \sigma_k) + K \eta (\sigma_i + \sigma_l)], \tag{15}$$

similarly to Eq. (6).

We can thus build up analogous extension processes of tensors, each of which contains an impurity tensor we have defined. The extension process of the impurity corner matrix that contains $A_{ij}^{(1)}$ is then written as

$$A_{(i_1 i_2)(j_1 j_2)}^{(n+1)} = \sum_{abcdef} C_{a j_2}^{(n)} X_{abc j_1}^{(n)} A_{fc}^{(n)} C_{db}^{(n)} X_{dei_1 f}^{(n)} C_{i_2 e}^{(n)}, \tag{16}$$

which is graphically shown in Fig. 6 (top left). Therein, the RG transformation $A_{(i_1 i_2)(j_1 j_2)}^{(n+1)} \to A_{ij}^{(n+1)}$ is depicted by the green lines with the open circles, which stand for U in accord with Eq. (13). The impurity tensor placed around the site B obeys the extension procedure

$$B_{(i_1 i_2)(j_1 j_2)}^{(n+1)} = \sum_{abcdef} C_{a j_2}^{(n)} X_{abc j_1}^{(n)} C_{fc}^{(n)} B_{db}^{(n)} X_{dei_1 f}^{(n)} C_{i_2 e}^{(n)}, \tag{17}$$
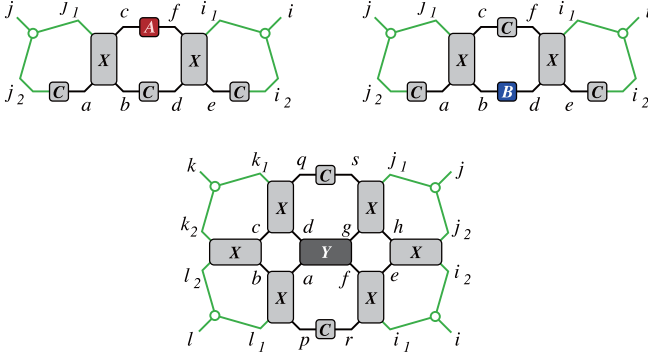
FIG. 6. Extension processes of the impurity tensor in Eq. (16) (top left), Eq. (17) (top right), and Eq. (18) (bottom). The RG transformations U are expressed by the external three green lines meeting at the open circles.

as shown on the top right of Fig. 6 (top right). For the location Y shown in Fig. 5, we take the contraction

$$
Y^{(n+1)}_{(i_1 i_2)(j_1 j_2)(k_1 k_2)(l_1 l_2)} = \sum_{\substack{abcdef \\ ghprqs}} X^{(n)}_{abl_1 p} X^{(n)}_{bck_2 l_2} X^{(n)}_{cdqk_1}
$$
$$
\times Y^{(n)}_{fgda} X^{(n)}_{efri_1} X^{(n)}_{ghj_1 s} X^{(n)}_{i_2 j_2 he} C^{(n)}_{rp} C^{(n)}_{sq}, \quad (18)
$$

which is depicted in Fig. 6 (bottom), where the graph is rotated by the right angle for bookkeeping.

In the calculation of the local bond energy $u(T)$, the initial tensors satisfy the equations

$$
A^{(1)}_{ij} = -\frac{J}{2}(\sigma_i + \sigma_j) \sum_{\xi} \xi \, \exp[K\xi(\sigma_i + \sigma_j)], \quad (19)
$$

$$
Y^{(1)}_{ijkl} = \sum_{\xi\eta} -J\xi\eta \, \exp[K(\sigma_i\sigma_j + \sigma_k\sigma_l + \xi\eta)]
$$
$$
\times \exp[K\xi(\sigma_j + \sigma_k) + \eta(\sigma_i + \sigma_l)], \quad (20)
$$

recalling that $B^{(1)}_{ij} = A^{(1)}_{ij}$. Starting the extension processes with these initial tensors, we can calculate the expectation value of the bond energy around site A by means of the ratio

$$
u_A(T) = \lim_{n\to\infty} \frac{\mathrm{Tr}\,(A^{(n)}[C^{(n)}]^3)}{\mathrm{Tr}\,([C^{(n)}]^4)}. \quad (21)
$$

The convergence with respect to n is fast because of the fractal geometry. It is straightforward to obtain the local energy $u_B(T)$ and $u_Y(T)$, as well as the local magnetization $m_A(T)$, $m_B(T)$, and $m_Y(T)$ in the same manner.

IV. NUMERICAL RESULTS

For simplicity, we use the temperature scale with $k_B = 1$ and fix the ferromagnetic interaction strength to $J = 1$. All the shown data are obtained after taking a sufficiently large number of system extensions, provided that the convergence with respect to n has been reached. The degrees of freedom D for each leg dimension is $D = 28$ at most. Apart from the critical (phase transition) region, where D needs to be the largest, we used $D = 18$, which sufficed to obtain the precise and converged data we have used for drawing all the graphs.
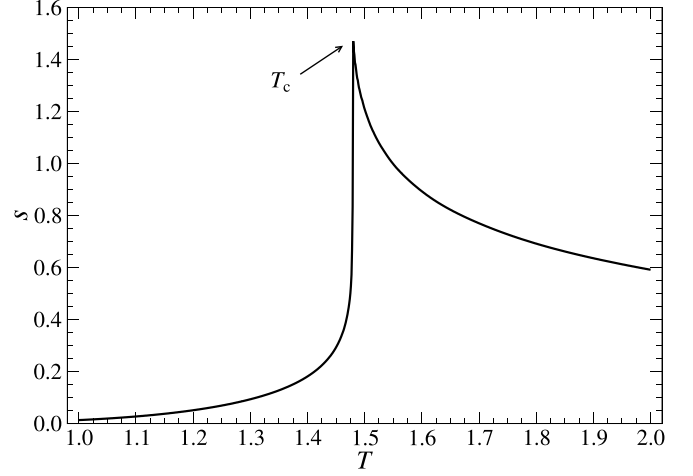

FIG. 7. The entanglement entropy $s(T)$ in Eq. (22).

An analogous kind of the entanglement entropy $s(T)$ can be calculated by the HOTRG method. After applying SVD to the extended tensor, $s(T)$ can be naturally obtained from the singular values ω_ξ in Eq. (11) through the formula

$$
s(T) = -\sum_{\xi} \frac{\omega_\xi^2}{\Omega} \ln \frac{\omega_\xi^2}{\Omega}, \quad (22)
$$

where $\Omega = \sum_{\xi} \omega_\xi^2$ normalizes the probability. The entanglement entropy $s(T)$ always exhibits stable convergence with respect to n. Figure 7 shows the temperature dependence of $s(T)$, which is obtained with $D = 18$. There is a sharp peak at the critical temperature T_c, which can be roughly determined as 1.48 from the data shown.

Taking the numerical derivative with respect to T for the calculated local energies $u_A(T)$, $u_B(T)$, and $u_Y(T)$, respectively, we obtain the specific heats $c_A(T)$, $c_B(T)$, and $c_Y(T)$, as shown Fig. 8. We observe a sharp peak in $c_Y(T)$ at T_c, whereas there is only a rounded maximum in $c_A(T)$ and $c_B(T)$, and their peak positions do not coincide with T_c
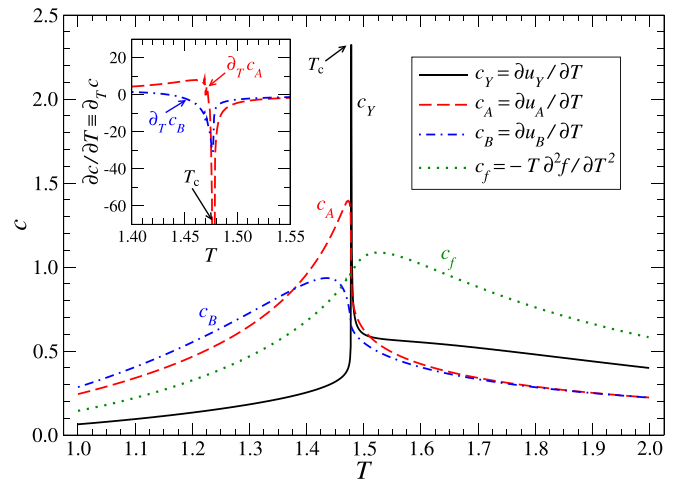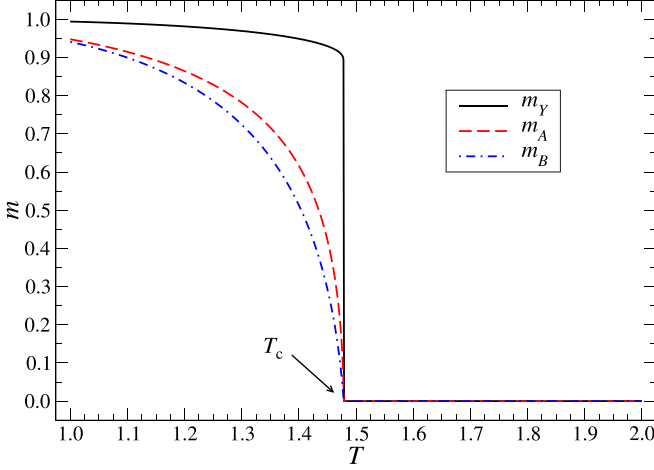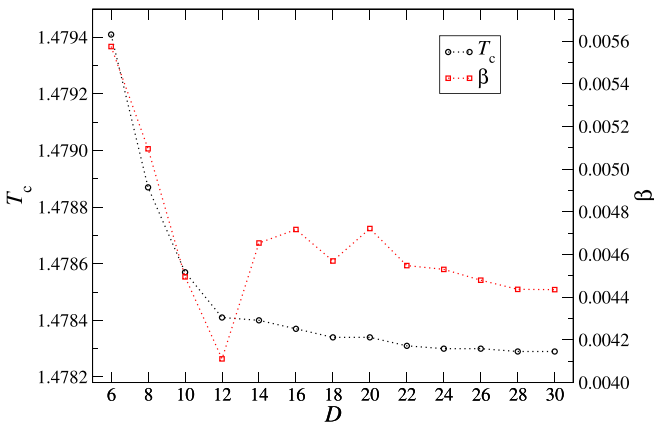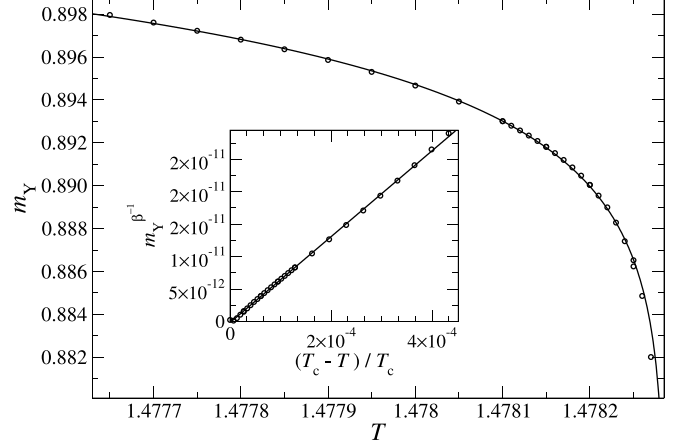

FIG. 8. Specific heats $c_A(T)$, $c_B(T)$, $c_Y(T)$, and $c_f(T)$. The inset shows the derivative of the specific heat with respect to temperature $\partial_T c$.

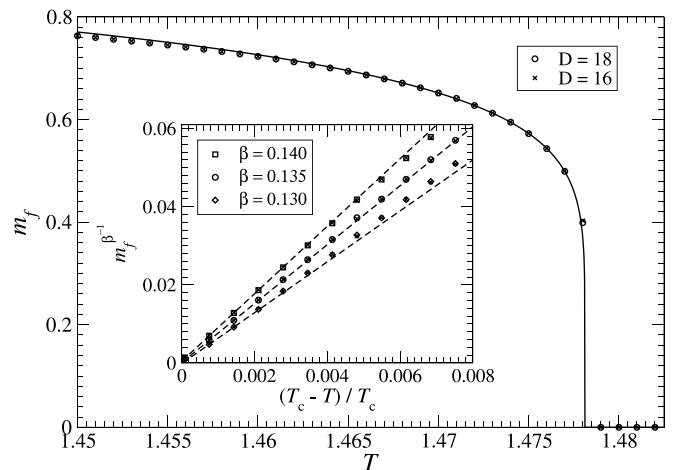FIG. 9. The local magnetization $m_Y(T)$, $m_A(T)$, and $m_B(T)$.

associated with position Y. The specific heat per site $c_f(T)$ defined in Sec. II as well as $c_A(T)$ and $c_B(T)$ demonstrate a weak singularity at T_c. This fact can be confirmed by taking their derivatives with respect to T, i.e., $\frac{\partial c}{\partial T}$, which leads to the identical singularity at T_c, as shown in the inset of Fig. 8. The result clearly manifests that the critical behavior strongly depends on the location, where the measurements of the bond energy are carried out.

Figure 9 shows the local magnetizations $m_A(T)$, $m_B(T)$, and $m_Y(T)$ with respect to temperature T, under the condition that $D = 18$. They fall to zero simultaneously at the identical T_c, while the critical exponent β in $m(T) \propto (T_c - T)^\beta$ is significantly different for each case. From the plotted $m_A(T)$, we obtain $\beta \approx 0.52$, and from $m_B(T)$ we obtain $\beta \approx 0.78$. In both cases, we use the rough estimate $T_c \approx 1.478$, and the data in the range $|T_c - T| < 0.015$ are considered for numerical fitting. Since the variation in $m_Y(T)$ is too rapid to capture β under the condition $D = 18$, we increase the tensor-leg freedom up to $D = 30$. As can be seen in Fig. 10, both critical temperature T_c and exponent β obtained from the local magnetization $m_Y(T)$ appear to be well converged when $D \gtrsim 28$. Figure 11 shows $m_Y(T)$ zoomed-in around

FIG. 11. Detailed view of $m_Y(T)$ when $D = 30$. Inset: The power-law behavior below $T_c = 1.47829$ plotted with the exponent $\beta = 0.0044(4)$.

$T \sim 1.478$. It should be noted that a small numerical error is strongly amplified in the temperature region $|T - T_c| \lesssim 10^{-5}$. Therefore, the data points in this narrow region were excluded from the fitting analysis. Then, we obtain $T_c \approx 1.47829$. The estimated critical exponent $\beta = 0.0044(4)$ is roughly two orders of magnitude smaller than β obtained from $m_A(T)$ and $m_B(T)$. In a similar manner, as we have observed for the specific heat, the critical behavior of the model strongly depends on the location of the impurity tensors A, B, and Y on the Sierpiński carpet.

The global spontaneous magnetization m_f calculated according to Eq. (10) using automatic differentiation is presented in Fig. 12. For $D = 18$, the fitting of $m_f(T)$ in the region $T \lesssim T_c$ yields $T_c \approx 1.478$ and $\beta \approx 0.135$. The relative difference between $D = 16$ and $D = 18$ in the estimate of β is around 0.1%. The linear dependence (dashed lines) of $m_f^{\beta^{-1}}$ below T_c is shown in the inset of Fig. 12.

FIG. 10. Critical temperature T_c (black circles) and critical exponent β (red squares) with respect to the bond dimension D obtained from the local magnetization $m_Y(T)$.

FIG. 12. The global magnetization $m_f(T)$ when $D = 16$ and $D = 18$. Inset: The power-law behavior below T_c.

V. CONCLUSIONS AND DISCUSSIONS

We have investigated the phase transition of the ferromagnetic Ising model on the Sierpiński carpet. The numerical procedures in the HOTRG method are modified, so they fit the recursive structure in the fractal lattice. We have confirmed the presence of the second-order phase transition, which is located around $T_c \approx 1.478$, in accordance with the previous studies [6–11]. Notably, the HOTRG method used in this study achieved numerical convergence of physical observables with $k \sim 35$ iterative extensions (generations) of the system, which is significantly higher than the maximum value of $k \leqslant 8$ reached by Monte Carlo studies. This demonstrates the effectiveness of the HOTRG method for studying phase transitions on fractal lattices. Moreover, the global behavior of the entire system captured by the free energy per site $f^{(\infty)}$ exhibits the presence of a very weak singularity at T_c, as we observed in Ref. [16].

What is characteristic of this fractal lattice is the position dependence in the local magnetization $m(T)$ and local energy $u(T)$. For example, we find that the critical exponent β differs by a couple of orders of magnitude, which corresponds to the fact that the measured magnetization depends on position, where the impurity tensor is placed on the fractal lattice. A key feature appears in the local energy $u_Y(T)$, where we deduce a sharp peak in its temperature derivative, $c_Y(T)$, contrary to the smooth behavior in $c_f(T)$, being the averaged specific heat. Intuitively, such a position dependence would be explained by the density of sites around the pinpointed location. Around site Y, the spins are interconnected more densely than those around boundary sites A and B in Fig. 5. One might find a similarity with the critical behavior on the Bethe lattice [23,24], where the singular behavior is only visible inside the system, whereas the free energy is represented by an analytic function of T for the entire lattice. Lastly, let us also mention that the position dependence of the critical exponents we observed in this study is analogous to the surface critical behavior captured by boundary tensor network methods in Refs. [25,26].

Finally, we leveraged automatic differentiation to compute the global spontaneous magnetization $m_f(T)$, which represents the average magnetization over all site locations. This approach allowed us to overcome the challenges associated with averaging impurities over all site locations on the fractal lattice. Our analysis revealed that the associated global critical exponent $\beta \approx 0.135$, which is intermediate between the local exponents associated with m_A ($\beta \approx 0.52$) and m_B ($\beta \approx 0.78$) on the one hand and m_Y ($\beta \approx 0.004$) on the other hand, but much closer to the former. Notably, the global critical exponent we report in this paper is consistent with estimates from previous Monte Carlo studies, as reported in the literature [6–8,10–12]. Our findings have important implications for understanding the critical behavior of magnetic systems on fractal lattices and could guide future experimental and theoretical investigations.

The current study can be extended to other fractal lattices, e.g., variants of the Sierpiński carpet or a fractal lattice we had already studied earlier [16], where the positional dependence of the impurities has not been examined yet. Another point to consider is to investigate more variations of the locations on the fractal lattice to analyze the mechanism of the nontrivial position-dependent behavior we observed.

APPENDIX A: EFFICIENT MODEL REPRESENTATION AND RG TRANSFORMATION

Here, we define a computationally more efficient tensor network representation introduced in the main text. This is achieved by replacing the corner matrix C by its two halves and reexpressing the fourth-order tensor X in terms of two third-order tensors. Using this approach, the overall computational cost is reduced from $O(D^{10})$ to $O(D^8)$ and the memory cost is reduced from $O(D^8)$ to $O(D^6)$, where D is the bond dimension cutoff.

1. Initialization

At initial step $n = 1$, we define left and right halves of the corner matrix [cf. Eq. (3)],

$$C_{ij}^{(1),+} = \exp[K(\sigma_a + \sigma_b)] \tag{A1}$$

and

$$C_{ij}^{(1),-} = \exp[K(\sigma_b + \sigma_a)], \tag{A2}$$

respectively, where the matrix indices $i = (\sigma_a + 1)/2$ and $j = (\sigma_b + 1)/2$ take the value either 0 or 1. Notice that the (left half) C^+ is indexed left to right whereas the (right half) C^- is indexed right to left, as seen in Fig. 13.

At the same time, we initialize the two halves (i.e., third-order tensors) of the X region (i.e., fourth-order tensor) as follows [cf. Eq. (6)]:

$$X_{ijk}^{(1),+} = \exp[K(\sigma_a\sigma_b + \sigma_b\sigma_c + \sigma_c\sigma_d + \sigma_d\sigma_a)], \tag{A3}$$

and

$$X_{ijk}^{(1),-} = \exp[K(\sigma_d\sigma_c + \sigma_c\sigma_b + \sigma_b\sigma_a + \sigma_a\sigma_d)], \tag{A4}$$

where k is a combined index obtained from c and d, i.e., $k = \sigma_c + 1 + (\sigma_d + 1)/2$, and it takes four integer values (0 to 3).
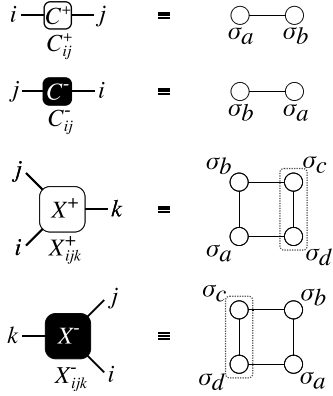
FIG. 13. Structure of the initial half-corner matrices $C^{(1),+}$ and $C^{(1),-}$ in Eqs. (A1)-(A2) and two 3-leg tensors $X_{ijk}^{(1),+}$ and $X_{ijk}^{(1),-}$ in Eqs. (A3) and (A4).

Notice that X^+ is indexed clockwise, whereas X^- is indexed anticlockwise, see Fig. 13.

2. Extensions

The extended corner-matrix halves $C^{(n+1),+}$ and $C^{(n+1),-}$ are

$$
\begin{aligned}
C_{ij}^{(n+1),+} &= C_{(i_1 i_2)(j_1 j_2)}^{(n+1),+} \\
&= \sum_{abcde} X_{i_1 ae}^{(n),+} X_{cbe}^{(n),-} C_{i_2 d}^{(n),+} C_{aj_2}^{(n),+} C_{bj_1}^{(n),+} C_{cd}^{(n),-} \quad \text{(A5)}
\end{aligned}
$$

and

$$
\begin{aligned}
C_{ij}^{(n+1),-} &= C_{(i_1 i_2)(j_1 j_2)}^{(n+1),-} \\
&= \sum_{abcde} X_{bce}^{(n),-} X_{ai_1 e}^{(n),+} C_{aj_2}^{(n),-} C_{bj_1}^{(n),-} C_{i_2 d}^{(n),-} C_{cd}^{(n),+}, \quad \text{(A6)}
\end{aligned}
$$

respectively, where the new indices i and j, represent the grouped indices $(i_1 i_2)$ and $(j_1 j_2)$, respectively, see lower row of Fig. 14.

Similarly, the extension relations for $X^{(n+1),+}$ and $X^{(n+1),-}$ are

$$
\begin{aligned}
X_{ijk}^{(n+1),+} &= X_{(i_1 i_2)(j_1 j_2)(k_1 k_2 k_3)}^{(n+1),+} \\
&= \sum_{\substack{abcdef \\ gmn}} X_{ni_1 g}^{(n),+} X_{i_2 j_2 e}^{(n),+} X_{j_1 mf}^{(n),+} \\
&\quad \times X_{dae}^{(n),-} X_{abf}^{(n),-} X_{bck_2}^{(n),-} X_{cdg}^{(n),-} C_{nk_3}^{(n),+} C_{mk_1}^{(n),-}, \quad \text{(A7)}
\end{aligned}
$$

$$
\begin{aligned}
X_{ijk}^{(n+1),-} &= X_{(i_1 i_2)(j_1 j_2)(k_1 k_2 k_3)}^{(n+1),-} \\
&= \sum_{\substack{abcdef \\ gmn}} X_{dae}^{(n),+} X_{cdg}^{(n),+} X_{bck_2}^{(n),+} X_{abf}^{(n),+} \\
&\quad \times X_{ni_1 g}^{(n),-} X_{i_2 j_2 e}^{(n),-} X_{j_1 mf}^{(n),-} C_{mk_1}^{(n),+} C_{nk_3}^{(n),-}, \quad \text{(A8)}
\end{aligned}
$$

where we have abbreviated the grouped indices to $i = (i_1 i_2)$, $j = (j_1 j_2)$, $k = (k_1 k_2)$, and $l = (l_1 l_2)$, see the upper row of Fig. 14.
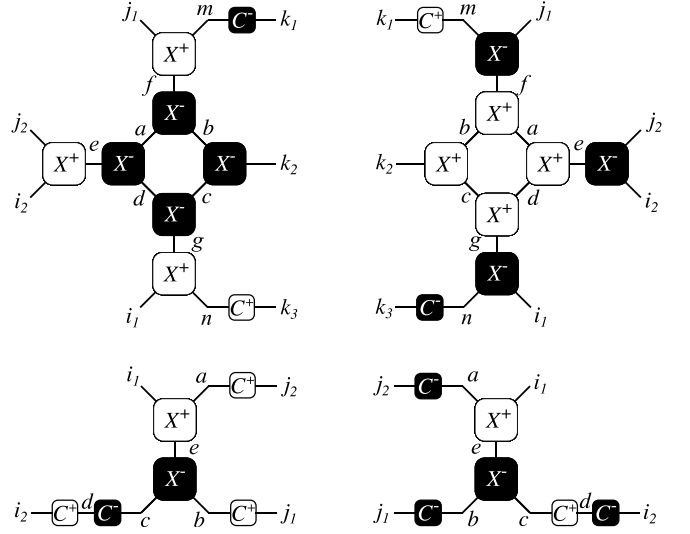

FIG. 14. The extension of the half-corner matrices $C^{(n),+}$ (lower left) and $C^{(n),-}$ (lower right) according to Eqs. (A5) and (A6), respectively, and the tensors $X^{(n+1),+}$ (upper left) and $X^{(n+1),-}$ (upper right) according to Eqs. (A7) and (A8), respectively.

3. Mapping to the original model representation

The full corner matrix $C^{(n)}$ and the tensor $X^{(n)}$ can be obtained at each step n of the iterative extension process in a straightforward way:

$$
C_{ij}^{(n)} = \sum_k C_{jk}^{(n),+} C_{ki}^{(n),-} \quad \text{(A9)}
$$

and

$$
X_{ijkl}^{(n)} = \sum_q X_{lkq}^{(n),+} X_{ijq}^{(n),-}, \quad \text{(A10)}
$$

respectively. This relation is depicted in Fig. 15.

4. RG transformation

First, we reshape the extended tensor $X_{(i_1 i_2)(j_1 j_2)(k_1 k_2 k_3)}^{(n+1),+}$ into a matrix $\tilde{X}_{(i_1 i_2)(j_1 j_2 k_1 k_2 k_3)}^{(n+1),+}$. The projector U is calculated using
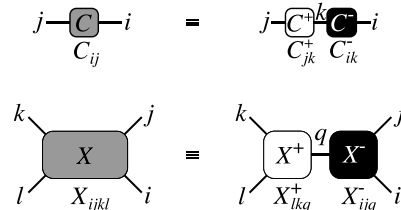

FIG. 15. Upper row: Mapping between the corner matrix C and its halves C^+ and C^- in Eq. (A9). Lower row: Mapping the tensor X and its halves X^+ and X^- (lower row) in Eq. (A10).
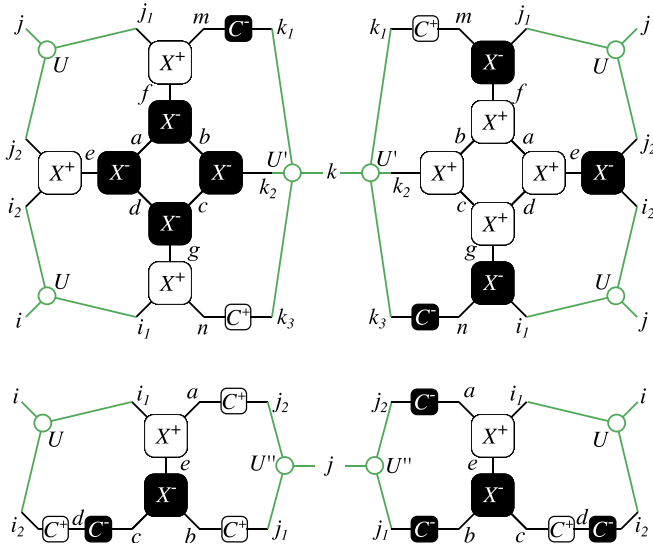
FIG. 16. The renormalization group transformations in Eq. (A14) (lower left), Eq. (A15) (lower right), Eq. (A16) (upper left), and Eq. (A17) (upper right).

the SVD applied to $\tilde{X}^{(n+1),+}$:

$$\tilde{X}^{(n+1),+}_{(i_1 i_2)(j_1 j_2 k_1 k_2 k_3)} = \sum_{\xi=1}^{D} U_{(i_1 i_2)\xi} \, \omega_\xi \, V_{(j_1 j_2 k_1 k_2 k_3)\xi}. \quad (A11)$$

To truncate the degrees of freedom associated with the grouped index $k = (k_1 k_2 k_3)$, we perform SVD on matrix

$$\tilde{\tilde{X}}^{(n+1),+}_{(k_1 k_2 k_3)(i_1 i_2 j_1 j_2)} = X^{(n+1),+}_{(i_1 i_2)(j_1 j_2)(k_1 k_2 k_3)},$$

$$\tilde{\tilde{X}}^{(n+1),+}_{(k_1 k_2 k_3)(i_1 i_2 j_1 j_2)} = \sum_{\xi=1}^{K_1} U'_{(k_1 k_2 k_3)\xi} \, \omega'_\xi \, V'_{(i_1 i_2 j_1 j_2)\xi}, \quad (A12)$$

where the sum corresponds to the largest K_1 singular values. Lastly, we prepare a projector for the grouped index $j = (j_1 j_2)$ in $\tilde{C}^{(n+1),+}_{(j_1 j_2)(i_1 i_2)} = C^{(n+1),+}_{(i_1 i_2)(j_1 j_2)}$,

$$\tilde{C}^{(n+1),+}_{(j_1 j_2)(i_1 i_2)} = \sum_{\xi=1}^{K_2} U''_{(j_1 j_2)\xi} \, \omega''_\xi \, V''_{(i_1 i_2)\xi}, \quad (A13)$$

where the sum corresponds to the largest K_2 singular values.

The RG transformation is then performed using the three different projectors U, U', and U'' as follows (see Fig. 16):

$$C^{(n+1),+}_{ij} \leftarrow \sum_{i_1 i_2 j_1 j_2} U_{(i_1 i_2) i} \, U''_{(j_1 j_2) j} \, C^{(n+1),+}_{(i_1 i_2)(j_1 j_2)}, \quad (A14)$$

$$C^{(n+1),-}_{ij} \leftarrow \sum_{i_1 i_2 j_1 j_2} U_{(i_1 i_2) i} \, U''_{(j_1 j_2) j} \, C^{(n+1),-}_{(i_1 i_2)(j_1 j_2)}, \quad (A15)$$

$$X^{(n+1),+}_{ijk} \leftarrow \sum_{\substack{i_1 i_2 j_1 j_2 \\ k_1 k_2 k_3}} U_{(i_1 i_2) i} \, U_{(j_1 j_2) j} \, U'_{(k_1 k_2 k_3) k}$$
$$\times X^{(n+1),+}_{(i_1 i_2)(j_1 j_2)(k_1 k_2 k_3)}, \quad (A16)$$

$$X^{(n+1),-}_{ijk} \leftarrow \sum_{\substack{i_1 i_2 j_1 j_2 \\ k_1 k_2 k_3}} U_{(i_1 i_2) i} U_{(j_1 j_2) j} \, U'_{(k_1 k_2 k_3) k}$$
$$\times X^{(n+1),-}_{(i_1 i_2)(j_1 j_2)(k_1 k_2 k_3)}. \quad (A17)$$

[1] M. S. Green and J. Lebowitz, in *Phase Transitions and Critical Phenomena*, edited by C. Domb (Academic Press, New York, 1972–2001), Vols. 1–20.

[2] Y. Gefen, B. B. Mandelbrot, and A. Aharony, Phys. Rev. Lett. **45**, 855 (1980).

[3] Y. Gefen, Y. Meir, B. B. Mandelbrot, and A. Aharony, Phys. Rev. Lett. **50**, 145 (1983).

[4] Y. Gefen, A. Aharony, and B. B. Mandelbrot, J. Phys. A: Math. Gen. **16**, 1267 (1983).

[5] Y. Gefen, A. Aharony, and B. B. Mandelbrot, J. Phys. A: Math. Gen. **17**, 1277 (1984).

[6] J. M. Carmona, U. M. B. Marconi, J. J. Ruiz-Lorenzo, and A. Tarancón, Phys. Rev. B **58**, 14387 (1998).

[7] P. Monceau, M. Perreau, and F. Hébert, Phys. Rev. B **58**, 6386 (1998).

[8] P. Monceau and M. Perreau, Phys. Rev. B **63**, 184420 (2001).

[9] G. Pruessner, D. Loison, and K. D. Schotte, Phys. Rev. B **64**, 134414 (2001).

[10] M. A. Bab, G. Fabricius, and E. V. Albano, Phys. Rev. E **71**, 036139 (2005).

[11] M. A. Bab, G. Fabricius, and E. V. Albano, Physica A **388**, 370 (2009).

[12] P.-Y. Hsiao and P. Monceau, Phys. Rev. B **67**, 064411 (2003).

[13] T. W. Burkhardt and J. M. J. van Leeuwen, *Real-Space Renormalization*, Topics in Current Physics (Springer, Berlin, 1982), Vol. 30, and references therein.

[14] M. Perreau, Phys. Rev. B **96**, 174407 (2017), and references therein.

[15] Z. Y. Xie, J. Chen, M. P. Qin, J. W. Zhu, L. P. Yang, and T. Xiang, Phys. Rev. B **86**, 045139 (2012).

[16] J. Genzor, A. Gendiar, and T. Nishino, Phys. Rev. E **93**, 012141 (2016).

[17] J. Genzor, A. Gendiar, and T. Nishino, Acta Phys. Slov. **67**, 85 (2017).

[18] R. Krcmar, J. Genzor, Y. Lee, H. Čenčariková, T. Nishino, and A. Gendiar, Phys. Rev. E **98**, 062114 (2018).

[19] J. Genzor, A. Gendiar, and Y.-J. Kao, Phys. Rev. E **105**, 024124 (2022).

[20] H.-J. Liao, J.-G. Liu, L. Wang, and T. Xiang, Phys. Rev. X **9**, 031041 (2019).

[21] B.-B. Chen, Y. Gao, Y.-B. Guo, Y. Liu, H.-H. Zhao, H.-J. Liao, L. Wang, T. Xiang, W. Li, and Z.-Y. Xie, Phys. Rev. B **101**, 220409(R) (2020).

[22] L. De Lathauwer, B. de Moor, and J. Vandewalle, SIAM J. Matrix Anal. Appl. **21**, 1324 (2000).

[23] R. J. Baxter, *Exactly Solved Models in Statistical Mechanics* (Academic Press, London, 1982).

[24] R. Krcmar, A. Gendiar, K. Ueda, and T. Nishino, J. Phys. A: Math. Theor. **41**, 125001 (2008).

[25] S. Iino, S. Morita, and N. Kawashima, Phys. Rev. B **100**, 035449 (2019).

[26] S. Iino, S. Morita, and N. Kawashima, Phys. Rev. B **101**, 155418 (2020).